



Optothermal characterization of vanadium dioxide films by Infrared Thermography

R. Li Voti^{a,*}, K. Agharahimli^a, M. Misano^a, M.C. Larciprete^a, G. Leahu^a, F.A. Bovino^a, C. Sibilìa^a, T. Cesca^b, G. Mattei^b, F.V. Lupo^c, R. Macaluso^c

^a Sapienza University of Roma, Department SBAI, Via A. Scarpa 14, I-00161 Rome, Italy

^b University of Padova, Department of Physics and Astronomy, Via Marzolo 8, I-35131 Padova, Italy

^c University of Palermo, Department of Engineering, Viale delle Scienze, I-90128 Palermo, Italy

ARTICLE INFO

Keywords:

Emissivity
Phase transition
Thermochromic materials
Vanadium dioxide
Infrared Thermography
Pulsed laser deposition

ABSTRACT

The thickness of vanadium dioxide (VO₂) films is a crucial parameter for the study of their optical and thermal properties. In this paper we studied the effect of the film thickness on the thermal hysteresis loop during the phase transition of VO₂ deposited on a sapphire substrate by pulsed laser deposition (PLD), by the application of the Infrared Thermography technique. We measure the main thermal hysteresis parameters of VO₂ samples with different thicknesses in the LWIR range (8–14 μm) showing how the transition temperature during the heating and cooling cycles, and the width of the hysteresis loop, may change with thickness. We analyzed and compared the obtained results with, in situ Grazing Incidence X-Ray Diffraction (GI-XRD). A good agreement between the results obtained with the two techniques was found demonstrating the reliability of the IR Thermography as a quantitative characterization tool.

The results show that the structural and IR emissivity properties of the VO₂ layer exhibit a dynamic range dependent on the layer thickness due to a correlation with the crystalline grain size. This has important effects in view of a tailored energy management for the use of those materials as smart radiators or smart windows.

1. Introduction

The semiconductor-to-metal transition (SMT) of VO₂ is the key property making this material technologically appealing for many applications ranging from “smart windows” and plasmonic devices [1–5], to optical memories [6], ultrafast switching of infrared radiation and oxide electronics [7–10] just to mention some of them.

The phase transition in bulk single crystals from the low temperature monoclinic phase [11] to the high temperature rutile phase [12] occurs at 68 °C. The transition may be triggered thermally [13], optically by hole doping [14–17] or photoelectron injection [18], by strain [19] and by DC electric field [20], although the role of Joule heating in the last case is still under investigation [21]. The electronic and structural phase transitions are accompanied by a large change in electrical [22], optical and infrared properties [23].

The abrupt change in optical, electrical and structural properties makes VO₂ interesting for a wide range of applications. For example, the ultrafast change in optical properties has prompted the development of

silicon-based optical modulators [24–26], in which a patch of VO₂ is deposited in contact with an optical waveguide and used to modulate light propagation. The expansion of the unit cell along the c-axis that accompanies the structural phase transition has recently been employed to construct high-speed mechanical micromanipulators [27,28]. The integration of phase change materials (such as VO₂) with plasmonic and metamaterials will add indispensable functionality for device technologies [29]. The wide variety of VO₂ applications require knowledge of film behavior on a variety of substrates, for different film thicknesses and across multiple deposition processes. However, to date there has been no systematic comparison of the influence of substrate and deposition process on VO₂ optical performance and morphology. Morphology, defects and strain are known to be critical for tuning the phase transition [19,30–38], highlighting the importance of understanding the influence of the substrate and the deposition process.

In this paper we show through direct and quantitative IR Thermography how the film morphology and infrared emissivity evolve as a function of the VO₂ film thickness deposited by pulsed laser deposition

* Corresponding author.

E-mail address: roberto.livoti@uniroma1.it (R. Li Voti).

(PLD) onto a sapphire substrate. IR Thermography presents the advantage of a direct comparison among different samples with an accessible information about the infrared emissivity and to physical quantities (like the evolution of the transition temperature and of the hysteresis width) related to the heating and cooling cycles from room temperature to 90 °C. To validate the obtained results an *in-situ* Grazing Incidence X-Ray Diffraction (GI-XRD) has been also performed.

2. Materials and measurements

2.1. Samples fabrication

Vanadium dioxide thin films were realized by pulsed laser deposition (PLD) onto 2 cm × 2 cm sapphire substrates of 0.5 mm thickness at the oxygen pressure of 10⁻² mbar and at the temperature of 550 °C. The PLD system employed is described in detail elsewhere [39,40]. It uses a Q-switched tripled Nd:YAG laser (Quantel mod. YG78C20, λ = 355 nm) generating 6 ns width pulses with an energy of 60 mJ per pulse. The density of energy was maintained at 3.3 J cm⁻² and the repetition rate was 4 Hz. The VO₂ target was a 2-inch diameter, 0.25-inch-thick disk purchased by Testbourne Ltd, UK, (purity 99.99 %). Prior to the deposition, each substrate was cleaned in an ultrasonic bath with acetone, subsequently rinsed with isopropanol and then dried with compressed air. After cleaning, each substrate was introduced into a vacuum bell jar where oxygen gas can be kept at the assigned pressure. Deposition temperature was fixed through an electrical heater, on which the sample was clamped, and a PID temperature controller. After the deposition, each film thickness was assessed by Rutherford Backscattering Spectrometry (RBS) and double-checked by profilometry and Scanning Electron Microscopy (SEM).

Six VO₂ layers with different thicknesses were deposited (see Fig. 1): the thinner film of 53 nm (sample A) is obtained with only 6400 laser pulses, while the thicker film of 690 nm (sample F) is obtained with 70 680 laser pulses, as reported in Table 1.

2.2. Infrared Thermographic measurements in the LWIR band

Thermographic data are measured by an IR camera (CX320 COX Co., working in the LWIR range 8–14 μm). A schematic representation of the experimental setup is reported in Fig. 2. An aluminum heated plate with a programmable thermal controller is used to heat uniformly all the samples (PTC-100 MJ Research inc.). The temperature scan is set from 30 to 90 °C with a progressive temperature increase with step ΔT = 1 °C for the heating cycle and vice versa for the cooling cycle. Sample temperature scanning is performed in a quasi-steady state transformation,

Table 1

Experimental samples thickness measured by RBS vs. laser pulses number.

Sample	PLD Pulse N.	Thickness RBS (nm)
A	6400	53 ± 5
B	12 872	97 ± 10
C	25 424	250 ± 20
D	36 000	340 ± 30
E	50 000	410 ± 40
F	70 680	690 ± 70

achieved by linearly changing the sample temperature with time at a low speed of about 1 °C min⁻¹.

The heater plate is made of a massive aluminum block to keep uniform the temperature on the plate surface. A thermocouple is used to monitor the temperature changes on the emitting surface of the sample. The thermocouple voltage allows to measure the temporal changes of the real temperature of the samples. Such experimental apparatus has already been successfully used for IR characterization and emissivity measurement of various nanostructures and metamaterials [41–46].

All samples, placed on the top of the aluminum heater plate, kept the same temperature within a spatial gradient of less than 0.5 °C. This allows the emissivity of all samples to be measured at the same time and under the same experimental conditions. The samples are ordered counterclockwise with increasing film thickness from 53 nm to 690 nm (according to the direction of the arrow in Fig. 1) to further highlight possible differences in the metal-insulator transition properties.

From the optical image in Fig. 1, the effective deposition surface can be easily recognized by its dark color (the white areas identify uncoated zones of the sapphire substrate). Thermographic images of all the samples A, B, C, D, E, and F during the heating cycle for three different temperatures below and above the transition temperature (65, 68 and 75 °C) are shown in Fig. 3. The apparent temperature is measured by the IR camera by setting the reference background emissivity to ε_{ref} = 0.95, and the environmental temperature to 25 °C. Apparent temperature values can be estimated from the color bar on the right in Fig. 3.

It is worth noting that in the areas where VO₂ is deposited, the apparent temperature after the transition decreases strongly due to the drop of emissivity. This is well evidenced by the dark red color assumed at 75 °C by almost all the samples in the color maps in Fig. 3 with the only exception of sample A corresponding to the thinnest deposited vanadium oxide film (53 nm). The uniformity of VO₂ film thickness can be inferred from the uniformity of the color maps for each sample.

The apparent temperature was measured during a complete heating/cooling cycle from 30 °C to 90 °C for each sample. For simplicity and

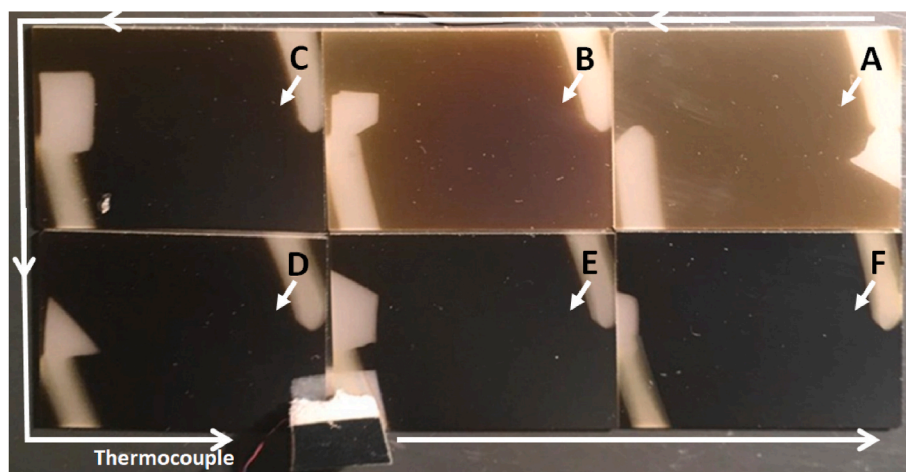


Fig. 1. Experimental arrangement of samples A, B, C, D, E and F corresponding to increasing VO₂ film thicknesses as measured by RBS technique (see Table 1). All samples are placed onto an Al plate to ensure temperature uniformity across the samples.

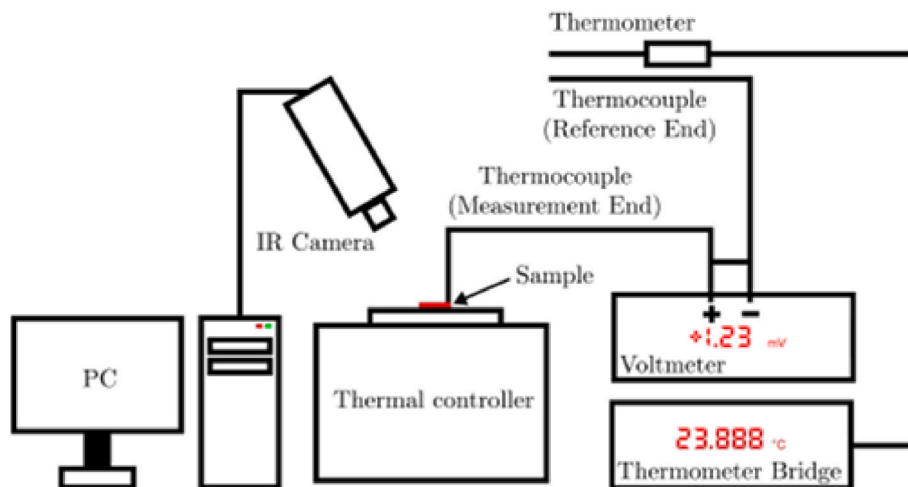


Fig. 2. Schematic representation of the experimental setup for IR thermography.

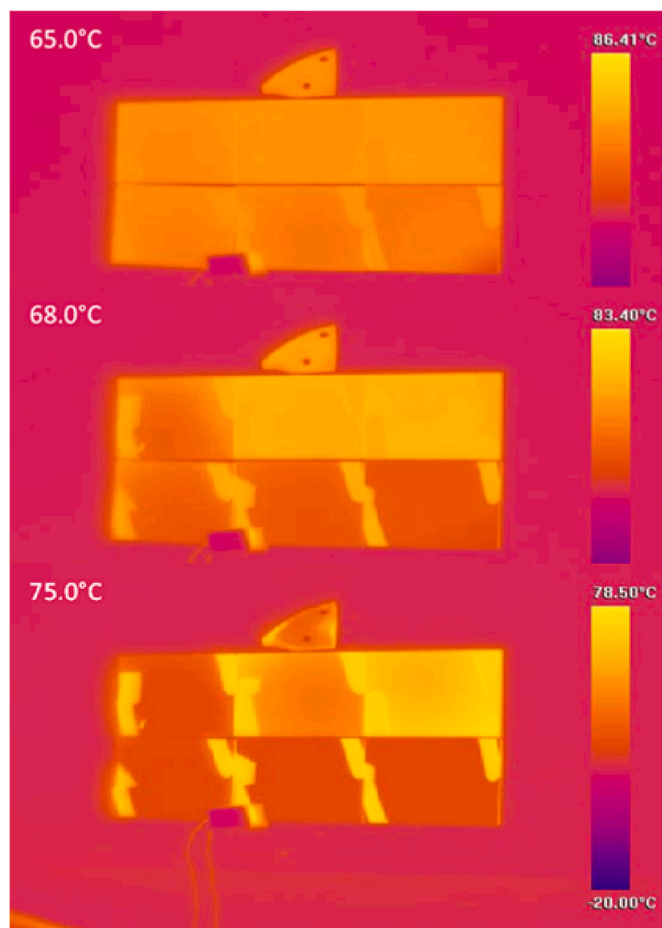


Fig. 3. Thermographic image of samples A, B, C, D, E, and F below and above the transition temperature (65, 68, and 75 °C) during the heating cycle. All samples are placed on an aluminum plate as described in Fig. 1. On the left is indicated the temperature measured by the thermocouple. On the right is displayed color map of apparent temperature measured by the IR camera.

without losing generality the apparent temperature has been averaged over the wide rectangular area located in the center of the sample surface (5 mm × 5 mm). As an example, Fig. 4 shows the averaged apparent temperature versus actual temperature (measured by the thermocouple) for the two samples with minimum (sample A), and maximum thickness

(sample F), as well as for the aluminum plate chosen as a reference. The hysteresis cycle is clearly visible for the VO₂ thin films (A in Fig. 4a and F in Fig. 4b), but obviously not for the reference aluminum plate (in Fig. 4c). In Fig. 4 the theoretical black dashed lines correspond to constant emissivity lines for a better understanding and delimitation of the emissivity range for each sample.

2.3. Structural and compositional characterizations

In-situ X-ray diffraction measurements as a function of the temperature are performed in grazing incidence (GIXRD, with grazing angle $\omega = 0.5^\circ$) and $\omega-2\theta$ geometry by using a Panalytical X'Pert Pro high-resolution diffractometer working in parallel beam geometry with a CuK α source. The system is equipped with an Anton Paar DHS900 heatable specimen holder. The measurements are taken in ambient air atmosphere, varying the temperature in the range 40–100 °C, at steps of 2 °C with a heating (cooling) rate of 0.4 °C min⁻¹, letting the system thermalize for 2 min at each temperature.

The composition and thickness of the samples were measured by Rutherford Backscattering Spectroscopy (RBS) using ⁴He⁺ ions with an energy of 2.2 MeV at the Van de Graaff Accelerator AN2000 of INFN-LNL Legnaro National Laboratories (Italy).

The sample roughness was measured with Atomic Force Microscopy (AFM) with an NT-MDT Solver Pro microscope.

3. Data analysis and discussion

3.1. Characterization of the VO₂ films and phase transition

In order to convert the number of laser pulses into a VO₂ film thickness, we performed RBS analysis, which confirmed also the correct stoichiometry of the films. We assumed for the VO₂ molecular density the one measured on similar samples made by PLD as $\rho = 34.1 \frac{\text{mol}}{\text{nm}^3}$ [23]. The results are reported in Table 1 and plotted in Fig. 5a, which shows a linear proportionality between number of laser pulses and measured thickness, with a slope $s = (9.4 \pm 0.3) \times 10^{-3} \text{ nm/pulse}$. The thickness measured with RBS has been also confirmed with cross-sectional FE-SEM electron microscopy images. The sample surface morphology was monitored with FE-SEM, showing the typical granular structure (reported in Fig. 5b for the sample F with a thickness of 690 nm), with grain size which gets larger as the film thickness increases.

A systematic structural characterization of the samples was performed with GIXRD X-ray diffraction. Fig. 5c shows the diffraction pattern measured at low (blue line) and high (red line) temperature in sample F, which is consistent with the monoclinic (M, semiconducting)

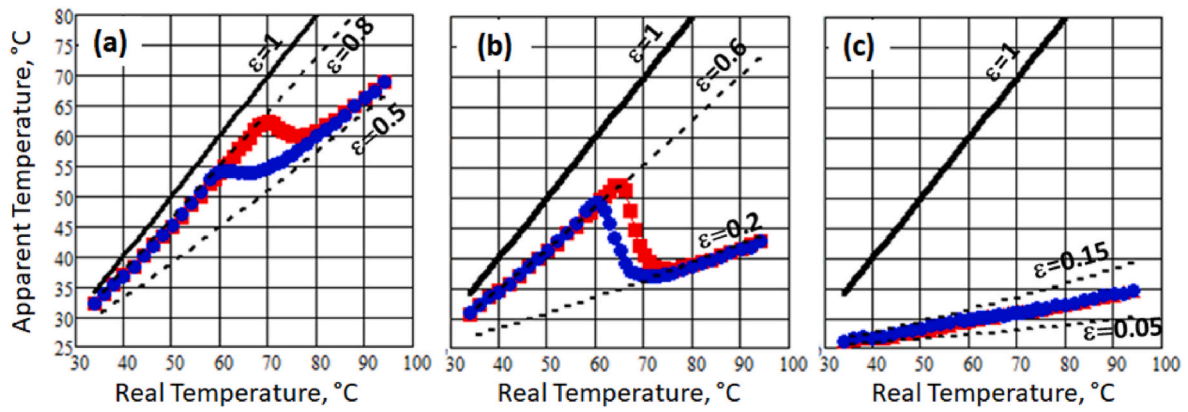


Fig. 4. Apparent temperature (IR camera) vs real temperature (thermocouple): (a) sample A (53 nm VO₂ thin film); (b) sample F (690 nm VO₂ thick film); (c) aluminum plate. The hysteresis loop is highlighted by the contrast between the experimental results obtained during the heating cycle ■ and cooling cycle ●. The apparent temperature has been averaged over the wide rectangular area located in the center of the sample surface (5 mm × 5 mm).

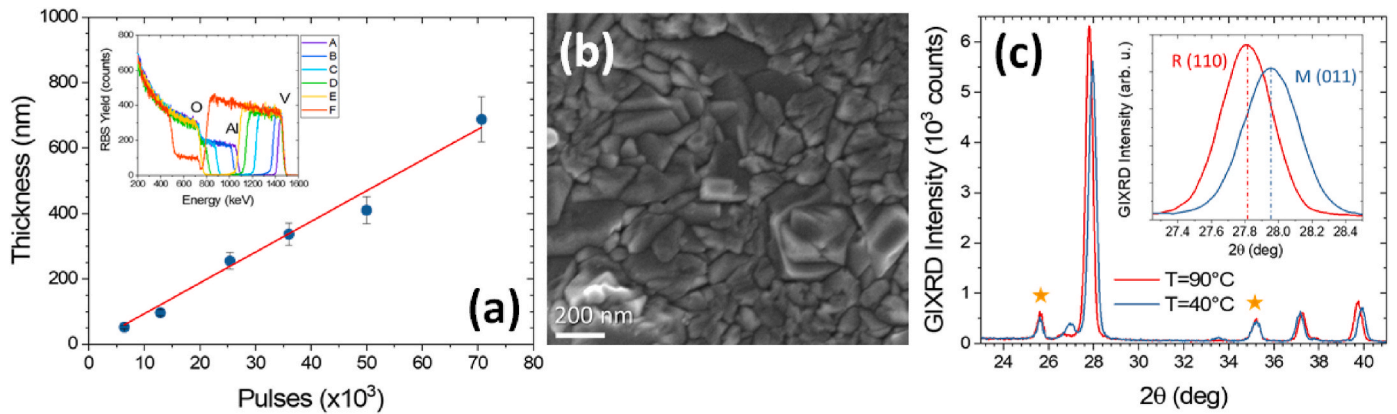


Fig. 5. Structural characterization: (a) calibration of the thickness vs. number of laser pulses as measured by RBS (in the inset the RBS spectra of the samples with the corresponding edges for V, Al and O signals in the sample A); (b) FE-SEM planar view of the sample F (70 680 pulses); (c) GIXRD measurement at $T = 40^\circ\text{C}$ (blue line) and $T = 90^\circ\text{C}$ (red line). The orange stars indicate Al₂O₃ substrate peaks. In the inset the close-up magnification showing the transition between (011) of monoclinic VO₂ (M, blue curve) and (110) rutile VO₂ (R, red curve) used to monitor the structural SMT transition.

phase of VO₂ at low temperature and of the rutile (R, metallic) phase at high temperature. From a quantitative analysis of the GIXRD spectra, following the same procedure reported in Ref. [23], we obtained the position of the centroid of the diffraction peak close to 28 deg as a function of the temperature for heating and cooling cycles. This involves the transition between (011) of monoclinic VO₂ (M) and (110) rutile VO₂ (R) used to monitor the structural SMT transition. The results are plotted in Fig. 6 for all the samples. All the cycles in Fig. 6 exhibit a clear transition temperature close to the expected one for the SMT in VO₂ and a hysteresis whose width decreases with the sample thickness. The curves were fitted with the same procedure as in Ref. [23]:

$$f_j(T) = \frac{f_h + f_l}{2} + \frac{f_h - f_l}{2} \operatorname{erf}\left(\sqrt{2} \frac{T - T_j}{\sigma_j}\right) \quad (1)$$

with $j = H, C$ for the heating (H) and cooling (C) cycle, respectively. $\operatorname{erf}(x)$ is the error function, f_h and f_l are the asymptotic high T and low T values of the function $f(T)$, whereas T_j and σ_j are the transition temperature and the width of the transition, respectively. The main parameters of the hysteresis cycles are summarized in Table 2.

The evolution of the hysteresis width, $\Delta T = T_H - T_C$, and of the difference in the transition widths, $\Delta\sigma = \sigma_C - \sigma_H$, as a function of the sample thickness are reported in Fig. 7 (a) and (b) as a function of the sample thickness. The experimental data (blue points) were fitted with a stretched exponential decay function (red line) $f(t) = \exp\left(-\left(t/t_c\right)^\beta\right)$

with stretching parameter β . In the case of the ΔT a perfectly exponential decay ($\beta = 1$) was found with a characteristic thickness length of $t_c \sim 150$ nm. For $\Delta\sigma$ a better fit is obtained with a stretching parameter of $\beta = 0.75$.

In general, the values of ΔT and $\Delta\sigma$ can be influenced by crystal grain size distribution, strain or defects [23]. To check whether this evolution can be related to a corresponding variation of the average grain size in the samples as a function of thickness, a Scherrer analysis of the diffraction peak width (with correction for the instrumental broadening) was performed for all the samples: the resulting average crystalline grain size (D) is reported in Fig. 7c.

Also, in this case a stretched exponential growth model gave a better fit with the same stretching factor $\beta = 0.75$, as found for $\Delta\sigma$. These results may indicate a correlation between the measured features of the hysteresis and the size distribution. Indeed, Fig. 7d and (e) report a linear evolution of ΔT and $\Delta\sigma$ as a function of the average crystalline size D .

3.2. Determination of emissivity by IR Thermography in the LWIR band

Infrared emissivity measurement methods can generally fall into two distinct categories: direct and indirect methods. Direct methods include calorimetry [48], the energy method [49], and the multi-wavelength method [50], whereas indirect methods are mostly based on reflectometry [51]. Numerous emissivity measuring instruments have been

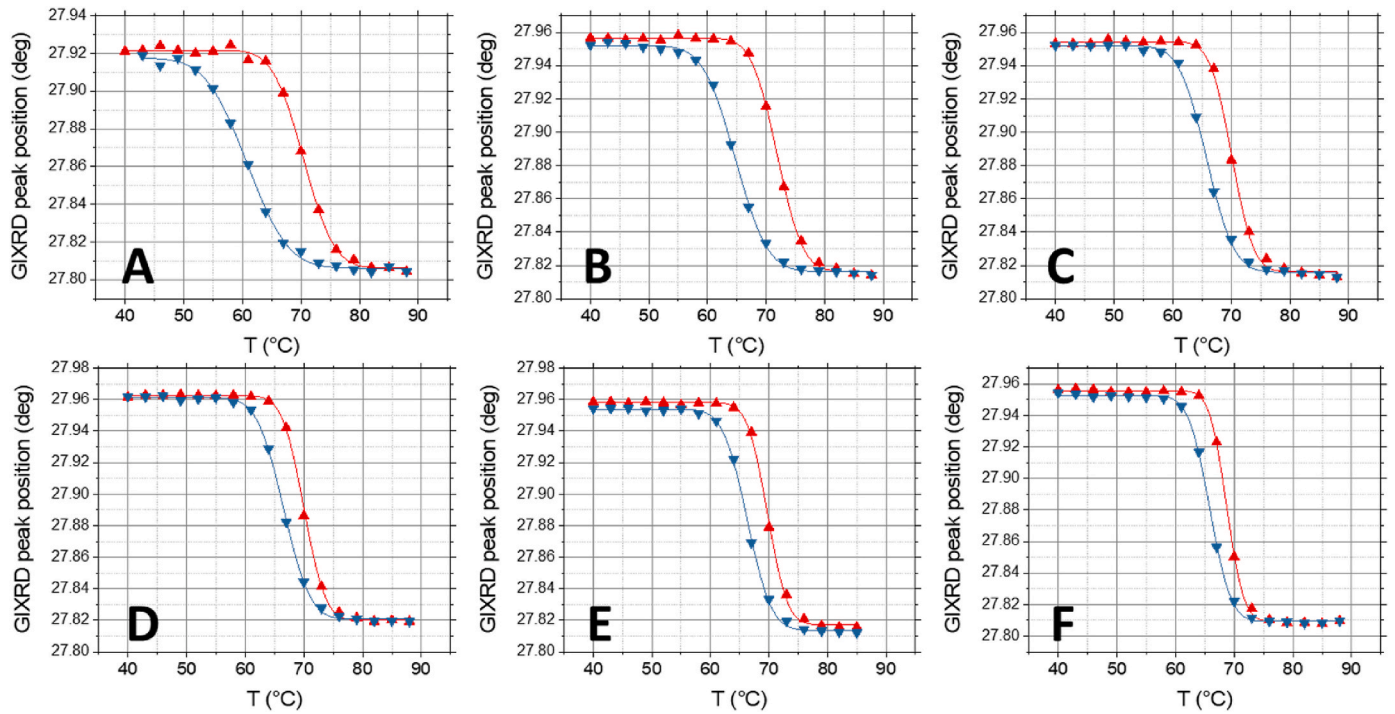


Fig. 6. Heating (red points) and cooling (blue points) cycles in the range $T = 40\text{ }^{\circ}\text{C} - 90\text{ }^{\circ}\text{C}$ for all the samples A to F. The points are the centroid of the diffraction peak close to 28 deg (inset of Fig. 5(c)), which represents the transition between (011) of monoclinic VO_2 (M) and (110) rutile VO_2 (R) used to monitor the structural SMT transition.

Table 2

Main hysteresis parameters obtained from structural (GIXRD) and optical (THERMOGRAPHY) measurements for the samples A, B, C, D, E, and F for different thickness of the VO_2 layer (measured by RBS). The mean values has been calculated by fitting the experimental data in Fig. 9 with a large number (100 000) of possible temperature-dependent emissivity profiles $\varepsilon(T)$ by choosing randomly the parameters in Eq. (5). The values reported in Tab.2 are obtained from the minimum of the reduced chi-squared distribution [47]. The standard deviation for each fitting parameter has been calculated from the inverse of the second derivative of the lowest parabolic envelope of the chi-squared distribution relative to the specific parameter. The accuracy is $\pm 0.2\text{ }^{\circ}\text{C}$ for all the transition temperatures T_H and T_C , $\pm 0.25\text{ }^{\circ}\text{C}$ for all the transition widths σ_H and σ_C , and ± 0.01 for the emissivity values ε_C , ε_H .

Sample	RBS thickness (nm)	GIXRD						IR THERMOGRAPHY							
		T_H ($^{\circ}\text{C}$)	T_C ($^{\circ}\text{C}$)	ΔT ($^{\circ}\text{C}$)	σ_H ($^{\circ}\text{C}$)	σ_C ($^{\circ}\text{C}$)	$\Delta\sigma$ ($^{\circ}\text{C}$)	ε_C	ε_H	T_H ($^{\circ}\text{C}$)	T_C ($^{\circ}\text{C}$)	ΔT ($^{\circ}\text{C}$)	σ_H ($^{\circ}\text{C}$)	σ_C ($^{\circ}\text{C}$)	$\Delta\sigma$ ($^{\circ}\text{C}$)
A	53 ± 5	70.1	60.8	9.3	8.2	11.1	2.9	0.74	0.54	74.5	66.3	8.2	5.3	7.7	2.4
B	97 ± 10	71.9	64.7	7.2	6.9	8.6	1.7	0.75	0.31	72.4	64.9	7.5	5.0	6.2	1.2
C	250 ± 20	70.1	65.8	4.3	5.9	7.4	1.5	0.70	0.17	68.6	63.2	5.4	4.4	5.9	1.5
D	340 ± 30	70.0	66.5	3.5	5.8	7.1	1.3	0.65	0.16	68.5	64.0	4.6	4.3	5.3	1.0
E	410 ± 40	69.7	66.3	3.4	5.4	6.5	1.1	0.62	0.16	68.2	63.9	4.3	4.5	5.3	0.8
F	690 ± 70	68.7	65.8	2.9	4.6	5.7	1.1	0.61	0.19	68.2	64.3	3.9	4.1	4.6	0.5

designed based on these methodologies, which have achieved good measurement performance at high temperatures. However, these methods and instruments perform poorly when applied at room temperature, motivating the search for new emissivity measurement methodologies specific to the near-ambient temperature range.

Specifically for the evaluation of the VO_2 /sapphire emissivity in both the SWIR and LWIR range we recently applied an indirect method based on the measurements of IR reflectivity and transmissivity [23].

Instead in this section we wish to introduce a direct method, which estimates the infrared emissivity directly from the knowledge of apparent, real and environmental temperature measured by IR Thermography. The methodology can be briefly summarized in the following lines:

a) Once the background emissivity $\varepsilon_{\text{ref}} = 0.95$ and the environmental temperature T_{room} is set, the thermal imaging camera returns the infrared signal S_{IR} and calculates the apparent temperature T_{app} of the sample, according to the expression:

$$S_{\text{IR}} \sim \varepsilon_{\text{ref}} \cdot U(T_{\text{app}}) + (1 - \varepsilon_{\text{ref}}) \cdot U(T_{\text{room}}) \quad (2)$$

where $U(T) = \int_{\lambda_{\text{min}}}^{\lambda_{\text{max}}} R(\lambda) \frac{2hc^2}{\lambda^5} \frac{1}{\exp(\frac{hc}{\lambda kT}) - 1} d\lambda$ is the integrated radiance of

the black body detectable by the IR camera, h the Planck's constant, k the Boltzmann's constant, c the speed of light in vacuum, $R(\lambda)$ is the IR detector responsivity, and $\lambda_{\text{min}} = 8\text{ }\mu\text{m}$ and $\lambda_{\text{max}} = 14\text{ }\mu\text{m}$ are the extremes of its wavelength bandwidth.

b) Once the real temperature is measured from the thermocouple, the S_{IR} infrared signal in Eq. (2) can be correlated to the effective emissivity of the sample, ε_S , by the expression

$$S_{\text{IR}} \sim \varepsilon_{\text{ref}} \cdot U(T_{\text{app}}) + (1 - \varepsilon_{\text{ref}}) \cdot U(T_{\text{room}}) = \varepsilon_S \cdot U(T_{\text{real}}) + (1 - \varepsilon_S) \cdot U(T_{\text{room}}) \quad (3)$$

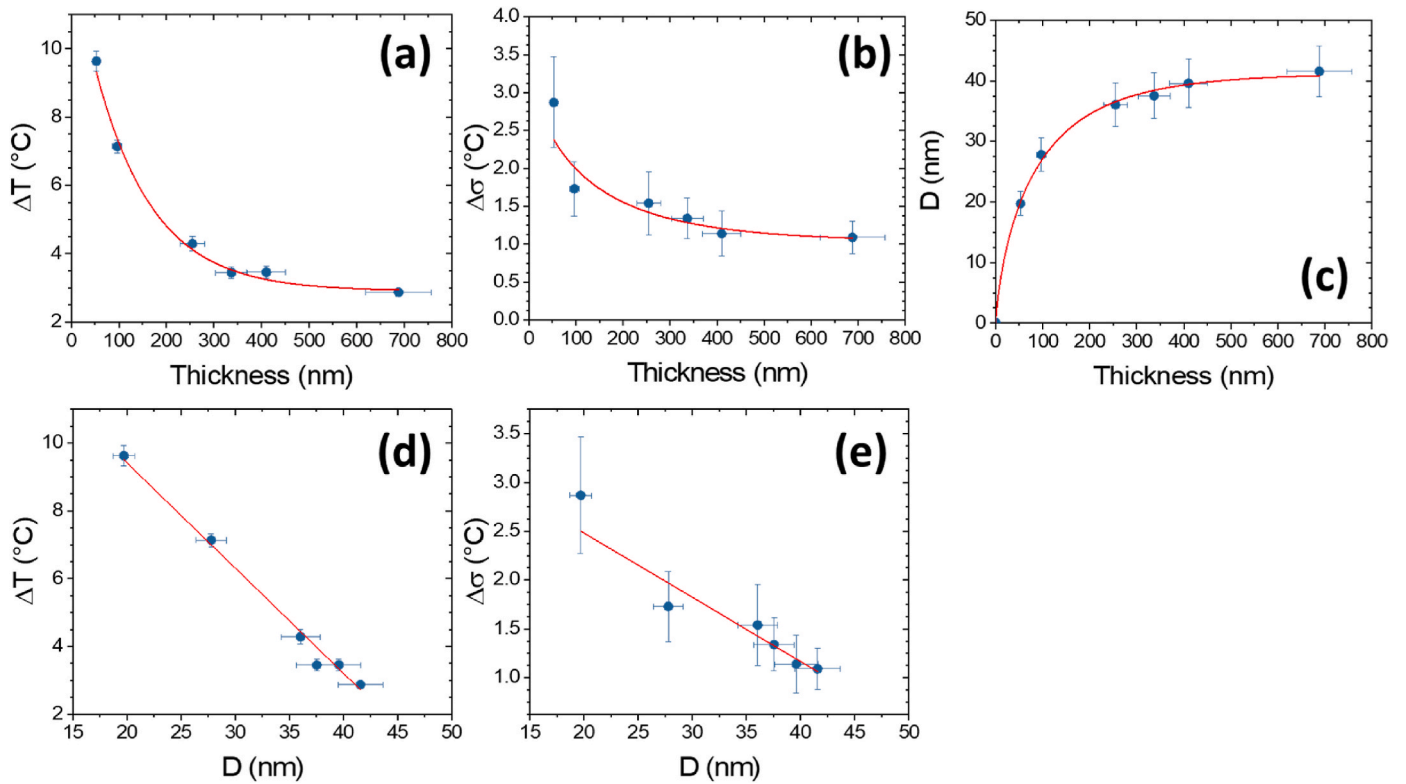


Fig. 7. (a) evolution of the hysteresis width (ΔT) as a function of the sample thickness; (b) evolution of the differences of the transition widths ($\Delta\sigma$) as a function of the sample thickness; (c) growth of the average crystalline grain size of the $M - VO_2$ phase as a function of the sample thickness; (d) ΔT as a function of the average diameter; (e) $\Delta\sigma$ as a function of the average diameter.

c) From Eq. (3) the emissivity ϵ_S of the sample can be easily calculated as follows [41,42]:

$$\epsilon_S = \epsilon_{ref} \frac{U(T_{app}) - U(T_{room})}{U(T_{real}) - U(T_{room})} \quad (4)$$

Such approach allows to measure directly the sample emissivity without applying comparative methods, which imply additional measurements on reference samples with known emissivity (i.e. graphite) [45,46,52,53].

It is worth noting that Eq. (4) is weakly dependent on the IR detector responsivity $R(\lambda)$. A simple proof is provided by the sensitivity test where R is chosen constant in the narrow range from 8 to 12 μm with

respect to the standard full range of LWIR. By comparing the results from the application Eq. (4) in the two cases (narrow vs full range), the difference for the estimated emissivity in the temperature range of 30 °C – 100 °C is always $|\Delta\epsilon_S| < 0.01$, that is lower than the uncertainty from the experimental measurements with our IR camera ($\Delta\epsilon = 0.01$).

Using Eq. (4), the thermographic images in Fig. 3 can be easily transformed into emissivity images, as shown in Fig. 8. It is worth noting that above the transition temperature (at 75 °C) the samples with thicker VO_2 films (samples C, D, E and F) show a uniform low emissivity (about $\epsilon = 0.20$), while for the thinner samples A, B, zones of non-uniform emissivity are clearly visible, probably corresponding to a non-uniform film growth. Also of interest are the changes in the emissivity

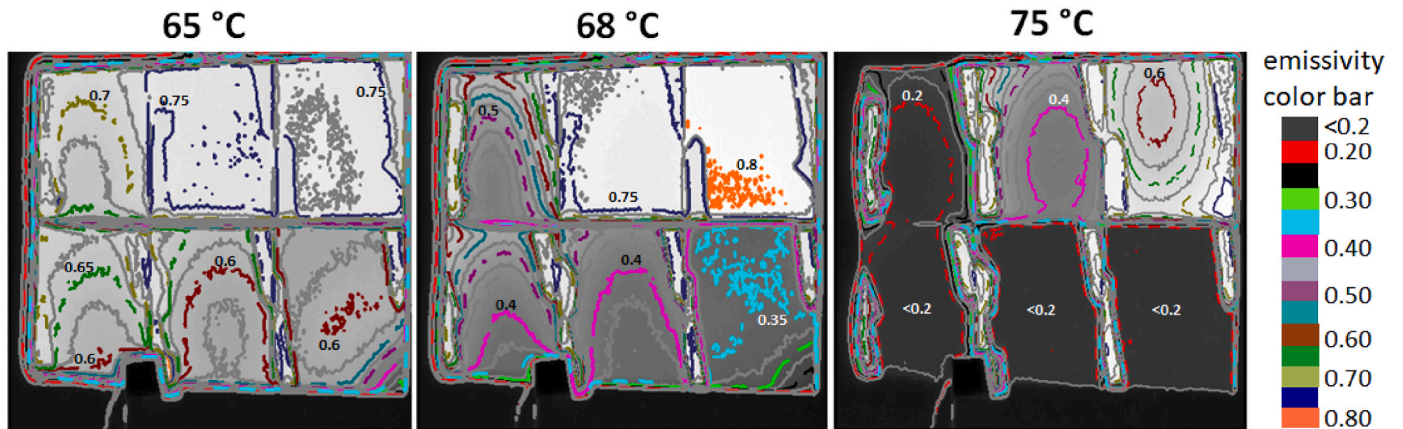


Fig. 8. Emissivity contour plot of samples A, B, C, D, E, and F below and above the transition temperature (65, 68, and 75 °C) during the heating cycle. The samples are placed on an aluminum plate as in Fig. 1. The emissivity contour plots are calculated from the thermographic images in Fig. 3 by using Eq. (4). On the right the emissivity color scale.

map observed at 68 °C, which may be related to the morphological change of the domains during the phase transition.

3.3. Parameters of thermal hysteresis

Other fundamental parameters of the thermal hysteresis are the transition temperatures during the heating and cooling cycles, T_H and T_C , and the corresponding hysteresis width $\Delta T = T_H - T_C$. These parameters can be calculated using the error function to simulate the phase transition as follows [23,54], similarly to Eq. (1):

$$\varepsilon(T) = \left(\frac{\varepsilon_H + \varepsilon_C}{2} \right) + \left(\frac{\varepsilon_H - \varepsilon_C}{2} \right) \cdot \text{erf} \left[\sqrt{2} \frac{(T - T_0)}{\sigma} \right] \quad (5)$$

where the $\varepsilon(T)$ is the temperature-dependent emissivity starting from ε_C to ε_H , the quantity T_0 is the transition temperature at which ε reaches 50 % of the emissivity change, and the transition width σ is the temperature range around T_0 within which 95 % of the phase transition occurs. By using Eq. (5) to analyze the emissivity experimental data at varying temperature shown in Fig. 9, the best-fit curves have been obtained, and the corresponding asymptotic hot and cold emissivity parameters (ε_H , ε_C), the transition temperatures T_H and T_C during the heating and cooling cycle respectively, and the corresponding width of the transition (σ_H , σ_C), can be determined, as shown in Table 2.

The main thermal hysteresis parameters as a function of VO_2 film thickness, measured by RBS technique on the A, B, C, D, E, and F samples, are summarized in Table 2 and plotted in Fig. 10. It is worth noting that the transition temperature during the heating cycle is at 68 °C, as expected, only for the vanadium dioxide films thicker than 200 nm (see red symbols in Fig. 10a), while for thinner films it increases as the thickness decreases, as shown in many recent works [23,55,56].

The width of the hysteresis $\Delta T = T_H - T_C$ also increases from 4 to 8 °C as the thickness decreases and the size of the VO_2 crystalline domains reduces (see Fig. 10b) [23]. The same broadening process also occurs for the transition width (see Fig. 10c), which represents the temperature range to complete the phase change process. It increases with the reduction of the film thickness.

3.4. Evaluation of the optical parameters of vanadium dioxide by IR Thermography

Table 2 shows also the infrared emissivity measured in the LWIR range (8–14 μm) by means of IR Thermography far from the phase transition, i.e., the emissivity values ε_C below the phase transition (at 40 °C) and the emissivity ε_H above it (at 90 °C). For all the samples, the quantity ε_C falls in the range 0.6–0.8 as expected. In fact, at 40 °C, VO_2 is in the semiconductor state, and the films are almost transparent in the LWIR making visible the emissivity of the sapphire substrate hidden underneath, which is about 0.76 (when measured with the IR camera in the LWIR range from 8 to 14 μm). Obviously, the transparency of vanadium dioxide decreases with thickness, and consequently ε_C also decreases with thickness. On the other hand, at 90 °C the emissivity ε_H tends to reach the minimum value of about 0.2 by increasing the film thickness. The main reason of this behavior is due to the switching of the VO_2 film to the metallic state, which implies about 80 % reflection of the infrared radiation if the VO_2 layer is thicker than 200 nm, as it happens for samples C, D, E, and F.

From the emissivity values measured by IR Thermography (for all samples except sample A which is too much inhomogeneous), knowing the layer thickness (measured by RBS), and taking from the literature the refractive index of the sapphire substrate in the LWIR range [57], it was then possible to calculate the refractive index of the vanadium dioxide film averaged in the LWIR range of the camera (8–14 μm). According to such a procedure it was possible to estimate the VO_2 complex refractive index in the semiconductor phase $\tilde{n}_C = n_C + i k_C = 1.6 + i 0.01$, (at 30 °C) in agreement with recent literature data [58]. Conversely, it was not possible to uniquely determine the VO_2 complex refractive index in the metal phase (at 90 °C) because of the significant absorption observed already in the 100 nm-thick films. In fact, it is well known that from a single emissivity measurement it is not possible to simultaneously determine the refractive index n and extinction coefficient k of a thick metal film. A simple demonstration is given by Eq. (6) for the emission normal to the surface:

$$\varepsilon_H = 1 - R_H = 1 - \left| \frac{n_H + i k_H - 1}{n_H + i k_H + 1} \right|^2 \quad (6)$$

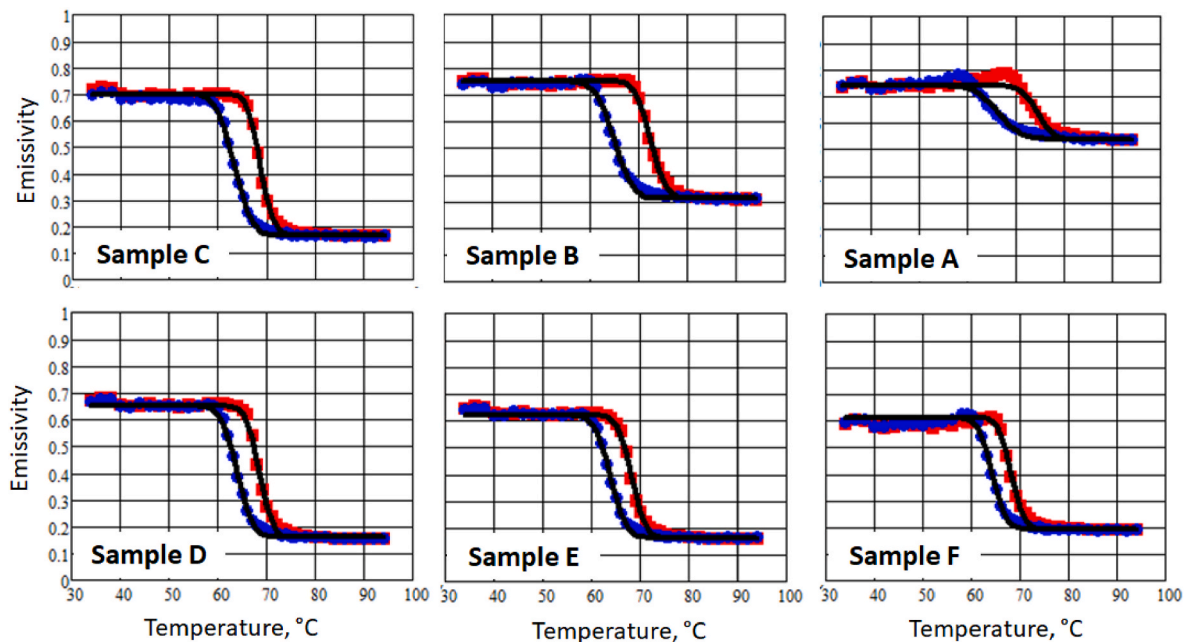


Fig. 9. Emissivity versus real temperature of vanadium dioxide thin films for samples A, B, C, D, E, and F. Emissivity is calculated by IR Thermography in the LWIR range (8–14 μm) using Eq. (4). The emissivity is eventually averaged over a wide rectangular area located in the center of the sample (5 mm \times 5 mm). ■ experimental data measured during the heating cycle; ● experimental data measured during the cooling cycle. The continuous black lines represent the best fit with Eq. (5).

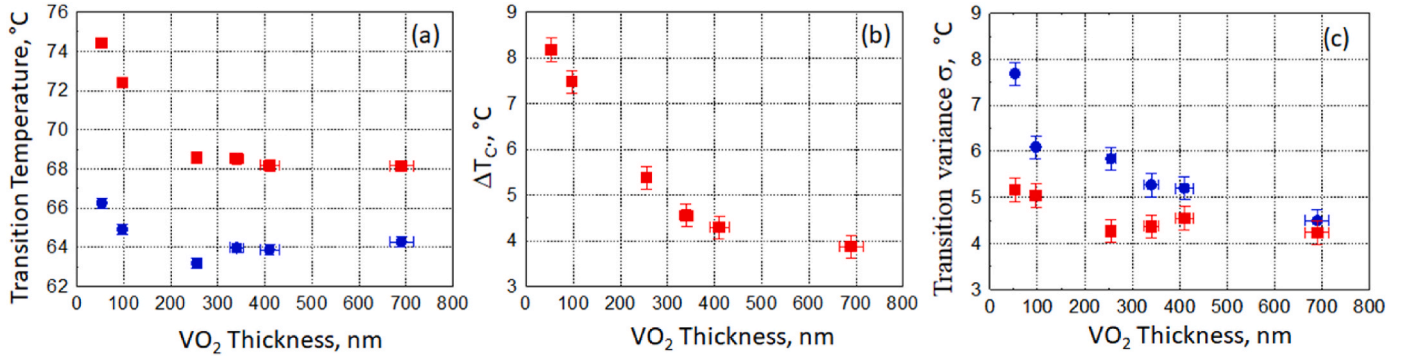


Fig. 10. Thermal hysteresis parameters for all samples ordered as a function of VO₂ thickness. (a) Transition temperature (■ heating cycle, ● cooling cycle); (b) hysteresis amplitude $\Delta T = T_H - T_C$; (c) transition width (■ heating cycle, ● cooling cycle).

where R_H is the sample reflectance for normal incidence that can be expressed in terms of the complex refractive index $\tilde{n}_H = n_H + i k_H$. n_H and k_H cannot be univocally determined from the knowledge of ε_H . In fact, there are infinite solutions for k_H , which can be expressed as a function of n_H and ε_H according to the formula:

$$k_H = \sqrt{\frac{4n_H}{\varepsilon_H} - (n_H + 1)^2} \quad (7)$$

Based on the possible solutions expressed by Eq. (7) and summarized in Fig. 11, the real part of the complex refractive index n_H and the corresponding imaginary part k_H have been set to $\tilde{n}_H = n_H + i k_H = 3 + i 7.1$ so to maximize the compatibility and the agreement with the data published in Ref. 58 for VO₂ films deposited by PLD onto a sapphire substrate (see Fig. 3 in Ref. [58]).

Accordingly, Fig. 12 shows the best fit between sample emissivity measurements (symbols) and theoretical calculations (solid lines) obtained by using the values described above for the refractive index of VO₂ in the semiconductor state at 30 °C (blue lines), and in the metallic state at 90 °C (red lines). It is worth noting that the thinner samples A and B in the metallic state are not in perfect agreement with the theoretical calculations. This could be ascribed to the inhomogeneity of thinner films, which, following a different growth regime than thicker films, have different densities and refractive indices than expected.

We now briefly summarize the main achievements and advantages of the approach followed in this section:

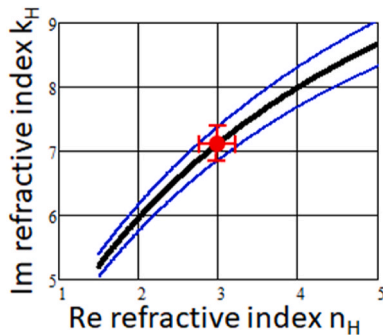


Fig. 11. Values of the real and imaginary part of the complex refractive index $\tilde{n}_H = n_H + i k_H$ of VO₂ in the metallic state (above transition temperature). The black curve was calculated from Eq. (7) for $\varepsilon = 0.18$ that is the value of hot emissivity averaged among the thickest samples (C, D, E, F). Being ± 0.01 the uncertainty associated to the emissivity measurements, the blue curves are calculated for $\varepsilon = 0.17$ and $\varepsilon = 0.19$ to show the propagation of the uncertainty on the refractive index. The value of $n_H + i k_H = 3 + i 7.1$ maximize the agreement with data of ref [58].

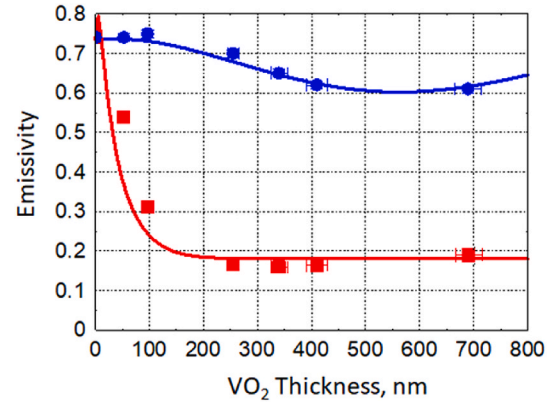


Fig. 12. Infrared emissivity in the LWIR range as a function of the thickness of the vanadium dioxide thin films. Theoretical predictions are calculated at 40 °C (blue line) with $\tilde{n}_C = 1.6 + i 0.01$, and at 90 °C (red line) with $\tilde{n}_H = 3 + i 7.1$ [58]. Experimental data on ε_C ●, and on ε_H ■ are taken from Table 2.

- i) From IR emissivity measurements at 40 °C of samples with different thicknesses (A,B,C,D,E,F) the refractive index \tilde{n}_C of vanadium dioxide averaged in the LWIR range has been calculated from the best fit shown in Fig. 12. The value \tilde{n}_C is unique for all samples and in agreement with the literature values in Ref.53, which are obtained on similar samples (PLD VO₂/Sapphire) by ellipsometry in the same IR range.
- ii) The refractive index \tilde{n}_H of vanadium dioxide at 90 °C has been also evaluated from IR emissivity by using Eq. (7). In such a case the intrinsic uncertainty shown in Fig. 11 has been removed with the a-priori information on the expectation values chosen in agreement with Ref.58.
- iii) The values found for \tilde{n}_C and \tilde{n}_H are representative specifically for PLD deposition process and can be used to improve the design and the optimization of VO₂ based multilayer nanostructures and metasurface for “smart” temperature controlled IR filters and relative devices [59].
- iv) The values of the hysteresis parameters reported in Section 3.3, again with IR Thermography, add relevant information on the (thickness dependent) transition temperature dynamics, useful for tailoring the control parameters of the devices.

4. Conclusions

The influence of the thickness of VO₂ films on their thermo-optical properties, as thermal emissivity, has been analyzed. For this purpose, the Infrared Thermography technique has been applied in the LWIR spectral range of the semiconductor-to-metal transition of VO₂ films

with increasing thickness in the range 50–700 nm; VO₂ films have been realized by Pulsed Laser Deposition on alumina substrates. In-situ GIXRD X-ray diffraction has been also utilized to validate and to support results of the Infrared Thermography. In fact, the results of the present study indicate that the thermo-optical properties of the VO₂ films deposited on a sapphire substrate by PLD are sensitive to the film thickness and to the average crystalline grain size. In particular an exponential saturation of the infrared properties as a function of the thickness with a characteristic thickness $t_c \sim 150$ nm has been found.

Quantitative analysis demonstrated that the Infrared Thermography technique can be used as a “low cost” imaging tool allowing to access to physical quantities (as for example the dynamic range of the transition temperature and of the hysteresis width) related to the heating and cooling cycles from room temperature to 90 °C.

These results are very important for the application of VO₂ thin films for smart radiators and smart windows, where the emissivity should be accurately manipulated and controlled for tailored energy management.

Declaration of competing interest

The authors declare that they have no known competing financial interests or personal relationships that could have appeared to influence the work reported in this paper.

Data availability

Data will be made available on request.

Acknowledgments

The authors acknowledge the Italian Ministry of Defense for granting the project PNRM “METEORE” (contract n. 564, year 2021).

References

- [1] Yanfeng Gao, et al., Nanoceramic VO₂ thermochromic smart glass: a review on progress in solution processing, *Nano Energy* 1 (2012) 221–246.
- [2] C. Granqvist, B. Pehlivan, Y.X. Ji, S.Y. Li, G. Niklasson, *Thin Solid Films* 559 (2013) 1.
- [3] T. Jostmeier, M. Mangold, J. Zimmer, H. Karl, H.J. Krenner, C. Ruppert, M. Betz, *Opt Express* 24 (2016), 17321.
- [4] N. Zheludev, Y. Kivshar, *Nat. Mater.* 11 (2012) 917.
- [5] M. Wang, Y. Xue, Z. Cui, R. Zhang, *J. Phys. Chem. C* 122 (2018) 8621.
- [6] H. Coy, R. Cabrera, N. Sepúlveda, F.E. Fernández, *J. Appl. Phys.* 108 (2010), 113115.
- [7] M. Soltani, M. Chaker, E. Haddad, R. Kruzelecky, J. Margot, P. Laou, S. Paradis, *J. Vac. Sci. Technol. A* 26 (2008) 763.
- [8] V.G. Golubev, V.Yu Davydov, N.F. Kartenko, D.A. Kurdyukov, A.V. Medvedev, A. B. Pevtsov, A.V. Scherbakov, E.B. Shadrin, *App.Phys.Lett.* 79 (2001) 2127.
- [9] D.A. Kurdyukov, S.A. Grudinkin, A.V. Nashchekin, A.N. Smirnov, E.Yu Trofimova, M.A. Yagovkina, A.B. Pevtsov, V.G. Golubev, *Phys. Solid State* 53 (2011) 428.
- [10] Z. Yang, C. Ko, S. Ramanathan, *Annu. Rev. Mater. Res.* 41 (2011) 337.
- [11] G. Anderson, *Acta Chem. Scand.* 10 (1956) 623.
- [12] S. Westman, *Acta Chem. Scand.* 15 (1961) 217.
- [13] F.J. Morin, *Phys. Rev. Lett.* 3 (1959) 34.
- [14] W. Roach, I. Balberg, *Solid State Commun.* 9 (1971) 551.
- [15] A. Cavalleri, C. Tóth, C.W. Squier, J.A. Squier, F. Ráksi, P. Forget, J.C. Kieffer, *Phys. Rev. Lett.* 87 (2001), 237401.
- [16] C. Kübler, H. Ehrke, R. Huber, R. Lopez, A. Halabica, R.F. Haglund, A. Leitenstorfer, *Phys. Rev. Lett.* 99 (2007), 116401.
- [17] S. Wall, D. Wegkamp, L. Foglia, K. Appavoo, J. Nag, R. Haglund Jr., J. Stahler, M. Wolf, *Nat. Commun.* 721 (2012).
- [18] K. Appavoo, B. Wang, N.F. Brady, M. Seo, J. Nag, R.P. Prasankumar, D.J. Hilton, S. T. Pantelides, R.F. Haglund, *Nano Lett.* 14 (2014) 1127.
- [19] J.H. Park, J. Coy, T. Kasirga, C. Huang, Z. Fei, S. Hunter, D. Cobden, *Nature* 500 (2013) 431.
- [20] H.T. Kim, B.G. Chae, D.H. Youn, G. Kim, K.Y. Kang, S.J. Lee, K. Kim, Y.S. Lim, *Appl. Phys. Lett.* 86 (2005), 242101.
- [21] B.A. Kruger, A. Joushaghani, J.K.S. Poon, *Opt Express* 20 (2012), 23598.
- [22] T. Yao, X. Zhang, Z. Sun, S. Liu, Y. Huang, Y. Xie, C. Wu, X. Yuan, W. Zhang, Z. Wu, G. Pan, F. Hu, L. Wu, Q. Liu, S. Wei, *Phys. Rev. Lett.* 105 (2010), 226405.
- [23] T. Cesca, C. Scian, E. Petronijevic, G. Leahu, R. Li Voti, G. Cesarini, R. Macaluso, M. Mosca, C. Sibilia, G. Mattei, *Nanoscale* 12 (2020) 851.
- [24] R.M. Briggs, I.M. Pryce, H.A. Atwater, *Opt Express* 18 (2010), 11192.
- [25] J.D. Ryckman, K.A. Hallman, R.E. Marvel, R.F. Haglund, S.M. Weiss, *Opt Express* 21 (2013), 10753.
- [26] P. Markov, J.D. Ryckman, R.E. Marvel, K.A. Hallman, R.F. Haglund, S.M. Weiss, in: *CLEO: 2013*, Optical Society of America, 2013. CTu2F.7.
- [27] K. Wang, C. Cheng, E. Cardona, J. Guan, K. Liu, J. Wu, *ACS Nano* 7 (2013) 2266.
- [28] A. Ra, F.E. Fernández, M.A. Hines, N. Sepúlveda, *J. Appl. Phys.* 107 (2010), 053528.
- [29] M.A. Kats, P. Blanchard, P. Genevet, Z. Yang, M.M. Qazilbash, D.N. Basov, S. Ramanathan, F. Capasso, *Opt. Lett.* 38 (2013) 368.
- [30] M.K. Liu, M. Wagner, E. Abreu, S. Kittiwatanakul, A. McLeod, Z. Fei, M. Goldflam, S. Dai, M.M. Fogler, J. Lu, S.A. Wolf, R.D. Averitt, D.N. Basov, *Phys. Rev. Lett.* 111 (2013), 096602.
- [31] M.M. Qazilbash, B. Brehm, G.O. Andreev, A. Frenzel, P.C. Ho, B.G. Chae, B.J. Kim, S.J. Yun, H.T. Kim, A.V. Balatsky, O.G. Shpyrko, M.B. Maple, F. Keilmann, D. N. Basov, *Phys. Rev. B* 79 (2009), 075107.
- [32] N.B. Aetukuri, A.X. Gray, M. Drouard, M. Cossale, L. Gao, A.H. Reid, R. Kukreja, H. Ohldag, C.A. Jenkins, E. Arenholz, K.P. Roche, H.A. Durr, M.G. Samant, S.S. P. Parkin, *Nat. Phys.* 9 (2013) 661.
- [33] S. Lysenko, F. Fernandez, A. Rua, H. Liu, *J. Appl. Phys.* 114 (2013), 153514.
- [34] K. Appavoo, D.Y. Lei, Y. Sonnefraud, B. Wang, S.T. Pantelides, S.A. Maier, R. F. Haglund, *Nano Lett.* 12 (2012) 780.
- [35] J.Y. Suh, R. Lopez, L.C. Feldman, R.F. Haglund, *J. Appl. Phys.* 96 (2004) 1209.
- [36] D. Ruzmetov, K.T. Zawilski, V. Narayanamurti, S. Ramanathan, *J. Appl. Phys.* 102 (2007), 113715.
- [37] Y. Zhao, J. Hwan Lee, Y. Zhu, M. Nazari, C. Chen, H. Wang, A. Bernussi, M. Holtz, Z. Fan, *J. Appl. Phys.* 111 (2012), 053533.
- [38] G. Beydaghyan, V. Basque, P. Ashrit, *Thin Solid Films* 522 (2012) 204.
- [39] M. Mosca, R. Macaluso, C. Cali, R. Butté, S. Nicolay, E. Feltin, D. Martin, N. Grandjean, *Thin Solid Films* 539 (2013) 55.
- [40] A. Boughelout, R. Macaluso, I. Crupi, B. Megna, M.S. Aida, M. Kechouane, *J. Electron. Mater.* 48 (2019) 4381.
- [41] I. Yuce, S. Canoglu, S.M. Yukseloglu, R. Li Voti, G. Cesarini, C. Sibilia, M. C. Larciprete, *Sensors* 22 (2022) 3918.
- [42] G. Cesarini, R. Li Voti, G. Leahu, A. Maurizi, M.C. Larciprete, M. Centini, G. Balleisio, W. Thida, C. Sibilia, *EOSAM, Rome* 13–17 (2021).
- [43] G. Cesarini, G. Leahu, A. Belardini, M. Centini, R. Li Voti, C. Sibilia, *Int. J. Therm. Sci.* 146 (2019), 106061.
- [44] G. Cesarini, G. Leahu, R. Li Voti, C. Sibilia, *Infrared Phys. Technol.* 93 (2018) 112.
- [45] M.C. Larciprete, Y.S. Gloy, R. Li Voti, G. Cesarini, G. Leahu, M. Bertolotti, C. Sibilia, *Int. J. Therm. Sci.* 113 (2017) 130.
- [46] M.C. Larciprete, A. Albertoni, A. Belardini, G. Leahu, R. Li Voti, F. Mura, C. Sibilia, I. Nefedov, I.V. Anoshkin, E.I. Kauppinen, A.G. Nasibulin, *J. Appl. Phys.* 112 (2012), 083503.
- [47] G. Leahu, R. Li Voti, M.C. Larciprete, C. Sibilia, M. Bertolotti, I. Nefedov, I. V. Anoshkin, *Int. J. Thermophys.* 36 (2015) 1349.
- [48] S. Krenek, D. Gilbers, K. Anhalt, D.R. Taubert, J. Hollandt, A dynamic method to measure emissivity at high temperatures, *Int. J. Thermophys.* 36 (2015) 1713–1725.
- [49] T. Iuchi, A. Gogami, Simultaneous measurement of emissivity and temperature of silicon wafers using a polarization technique, *Measurement* 43 (2010) 645–651.
- [50] P. Wang, Z. Xie, Z. Hu, Study on the multi-wavelength emissivity of GCr15 steel and its application on temperature measurement for continuous casting billets, *Int. J. Thermophys.* 37 (2016) 129.
- [51] C. Shao, K. Huan, Z. Li, W. Dong, J.-H. Wang, X.-Y. Song, Research on integrated blackbody emissivity measurement based on laser integral sphere reflectometry, *Acta Metrol. Sin.* 40 (2019) 427–431.
- [52] M.C. Larciprete, S. Paoloni, N. Orazi, F. Mercuri, M. Orth, Y. Gloy, M. Centini, R. Li Voti, C. Sibilia, *Int. J. Therm. Sci.* 146 (2019), 106109.
- [53] M.C. Larciprete, S. Paoloni, R. Li Voti, Y.S. Gloy, C. Sibilia, *Int. J. Therm. Sci.* 132 (2018) 168.
- [54] E. Robert, Robert Marvel, R. Harl, Valentin Craciun, Bridget R. Rogers, Richard F. Haglund, *Acta Mater.* 91 (2015) 217.
- [55] Currie Marc, D. Virginia, Wheeler, Downey Brian, Nepal Neeraj, B. Qadri Syed, A. James, Wollmershauser, Avila Jason, Nyakiti Luke, *Opt. Mater. Express* 9 (2019) 3717.
- [56] V.A. Klimov, I.O. Timofeeva, S.D. Khanin, E.B. Shadrin, A.V. Ilinskire, F. Silva-Andrade, *Tech. Phys.* 47 (2002) 1134.
- [57] M. Schubert, T.E. Tiwald, C.M. Herzinger, *Phys. Rev. B* 61 (2000) 8187.
- [58] Chenghao Wan, et al., *Z. Ann. Phys. (Berlin)* (2019), 1900188.
- [59] R. Li Voti, M.C. Larciprete, G. Leahu, C. Sibilia, M. Bertolotti, *J. Nanophotonics* 6 (2012), 061601.